Mesoscopic approach to fluid-solid interaction: Apparent liquid slippage and its effect on permeability estimation

Zi Li,[1,*] Sergio Galindo-Torres,[2] Alexander Scheuermann,[3] and Ling Li[1]

[1]*Research Group on Complex Processes in Geo-Systems, School of Civil Engineering, University of Queensland, Brisbane QLD 4072, Australia*

[2]*Department of Civil Engineering and Industrial Design, University of Liverpool, Liverpool L69 3BX, United Kingdom*

[3]*Geotechnical Engineering Centre, School of Civil Engineering, University of Queensland, Brisbane QLD 4072, Australia*

The liquid slippage behavior due to molecular interactions at fluid-solid (F-S) interfaces is of great importance to the transport of shale oil and clay water. A mesoscopic single-phase lattice Boltzmann method (LBM), based on a continuous and exponentially decaying F-S interaction force and a midgrid bounce-back boundary condition, is proposed to be responsible for the apparent liquid slippage. The F-S interaction force is established at the particle level and thus can be readily extended to porous media. When it is repulsive (attractive), the phenomena of positive (negative) slip lengths and fluid slip (damping) are successfully recovered. This model is validated by the velocity profiles on hydrophobic and hydrophilic surfaces in a benchmark microchannel flow experiment. The slip length is found to be independent of shear rate (its constituents including body force, pore diameter, and kinematic viscosity), but dependent on pore geometry (smaller in porous media than in capillary tubes). Both slip length and permeability ratio follow a power law relationship with interaction parameters (strength and decay length) in capillary tubes and porous media. The permeability ratio estimated analytically with the slip length considered agrees well with that calculated from the LBM simulations, except for the fluid slip in porous media with a significant overestimation. The estimated permeability ratio indicates that it increases (decreases) nonlinearly as the pore diameter decreases, suggesting the great importance of the F-S interaction particularly for thin capillary tubes and microporous media.

I. INTRODUCTION

The no-slip condition at fluid-solid (F-S) interfaces is always assumed for solving the Navier-Stokes (NS) equation in the continuum fluid mechanics [1]. Notwithstanding its lack of physical origin, the no-slip condition has received significant successes in a huge number of macroscale flow experiments. Nevertheless, a breakdown of the no-slip condition is inevitable with the onset of fluid slip. The liquid slippage (rather than gas slippage) is the focus of interest in this paper. Experimental evidence of apparent liquid slippage was initially indicated by measurements of the flow rate in thin capillary tubes with liquid-repellent solid surfaces [2–4], the velocity profile of microchannel flows [5–7], and the hydrodynamic force between the approaching solid surfaces in a liquid [8–10]. Later, numerical simulations based on the molecular dynamics (MD) simulation [11–13] and the mesoscopic lattice Boltzmann method (LBM) [14–16] were conducted to explore the relationship between amount of slip and wettability. Wu *et al.* [13] established a model of effective slip for the confined water flow, in terms of a linear sum of true slip and apparent slip, both of which are functions of contact angle induced by F-S interaction. Zhang and Kwok [16] related liquid slippage to a realistic F-S interaction and hence contact angle. Thorough reviews of investigation techniques

[17,18] and slip mechanisms [19–24] can be found. The slip lengths of typical hydrophobic surfaces range from tens of nanometers [10] to micrometers [5] and the flow enhancement ratios of thin channels vary from 1.05 [2] and 1.30 [3] to 100 [4].

The physical origin of no-slip (and fluid slip) is still a controversial subject. The molecular attraction between the liquid particles and the solid wall is thought to give rise to a bond leading to a no-slip boundary [25]. But this complete wetting system seems not to recognize the existence of adsorbed liquid layers so that a negative slip length is generated [26–28]. When this interaction strength becomes much weaker than that between the liquid molecules themselves, the liquid does not fully wet the solid and then slips over the solid surface [25]. This argument has been borne out by experimental evidence [2–10], but it is inadequate for the fact that the liquid can slip on hydrophilic surfaces [29–31]. What can be inferred from the verified observations [26–31] is that wettability is somewhat an ambiguous and insufficient index of hydrophobicity of a solid surface. Instead, the potentially essential factor may be the interaction force between liquid molecules and solid surfaces [11–16], which in some way can keep a consistency with wettability but avoid the limitation in contact angle restricted to between 0° and 180°. The F-S interaction, as a long-range surface force, is a few orders of magnitude larger than the van der Waals attraction force, and decays with the distance between liquid particles and solid walls. In fact, the F-S interaction force, responsible for

---

*Corresponding author: z.li@uq.edu.au

an apparent hydrophobic slippage, can be quantified by the difference between hydrodynamic forces on the hydrophilic surface with a no-slip boundary and on the hydrophobic surface [32]. Further, it is clearly recognized as an apparent extra attraction, which can be determined by the total force subtracting van der Waals attraction, hydrophobic attraction, and Reynolds drag [33]. Although a theoretical formula of the F-S interaction force is not given [32,33], the exponentially decaying function of hydrophobic attraction force between solid surfaces [34–36] may provide a useful analogy to the F-S interaction force in this work.

The fluid slip due to molecular F-S interactions is important to the transport properties of a liquid (oil or water) in micro- and nanoporous media. Javadpour *et al.* used the slip-corrected liquid permeability of the shale matrix to explain higher fluid loss during hydraulic fracturing [37]. They developed a flow equation to capture the coupled effects of pore geometry and slip condition in shale systems [38], and concluded that a slip boundary or a viscosity correction was necessary to describe the octane flow in quartz nanopores [39]. Lee *et al.* extended the investigations of slip effect to the water flow in parallel-walled fractures [40] and the transport of dense nonaqueous phase liquid [41] and water [42] in rough-walled fractures, which depended on wettability and aperture size.

In addition to positive slip lengths [5–16,29–31] and higher-than-expected water flow rates [2–4,37–42], the interaction between water molecules and solid surfaces can also result in negative slip lengths (fluid damping) [26–28] and reduced percolation capability of water in extremely low permeability reservoirs. The irreducible water saturation formed when water molecules are adsorbed on solid surfaces is difficult to be mobilized at a lower driving pressure, and its amount is a function of the driving pressure gradient [43]. The improved permeability estimation methods, such as the equivalent rock element model [44], the model for predicting petrophysical properties [45], and the fractal geometry theory [46,47], considered the irreducible water saturation. The adsorbed water layer may account for the following phenomena: (1) the pre-Darcy effect [48–50], in which the Darcy flux increases nonlinearly (more than proportionally) with the pressure gradient, and (2) threshold pressure gradient [51–53], below which the fluid does not flow. Longmuir [54] also attributed the non-Darcy behaviors to the quasicrystalline structure (equivalent to adsorbed water layer) due to the cohesive interaction between fluid molecules and solid surface, and offered a three-zone description for the low permeability reservoirs: (1) dead zone, (2) nonlinear seepage (pre-Darcy) zone, and (3) pseudolinear seepage (larger than threshold pressure gradient) zone.

Differently from phenomenological investigations of liquid slippage [2–7,37–47], the hydrodynamic force measurements using the surface force apparatus [8–10] and the numerical simulations based on MD simulation [11–13] and mesoscopic LBM approach [14–16] considered the physical origin of liquid slippage: the F-S interaction force. Compared with MD simulation based on the Lennard-Jones interactions, the mesoscopic LBM approach is advantageous in describing the mechanism of molecular interactions and allowing the simulation of microfluidic flow experiments. The LBM has

achieved great progress in the simulation of fluid behaviors [55] recently. With a parallelized architecture and the capability to treat complex boundaries, it can recover the NS equation for the bulk fluid and represent a no-slip boundary using the midgrid bounce-back boundary condition (BC). The early applications of LBM to study fluid slip on solid surfaces were performed by combining bounce-back and specular reflection BCs [56,57] and by relating the LBM relaxation time to the Knudsen number [58,59]. However, these LBM schemes did not directly link liquid slippage behavior with the F-S interaction. Such interaction was formulated in a way that the solid wall was treated as another fluid component in a multicomponent LBM with the midgrid bounce-back BC [14], but it acts within only one lattice unit and thus cannot fully deal with the profiles of velocity and density near the wall. Subsequently a continuous and decaying interaction with a distance from the wall was introduced to replace the local interaction [15,16,57], but it occurs between fluid particles and flat walls and thus cannot simulate the fluid slip and evaluate its influence on the permeability of a porous medium.

The purpose of this paper is to better understand the physics of molecular interactions at F-S interfaces and to assess its influence on the transport of shale oil and clay water. In this work, the physical behavior of a fluid near solid surfaces is modeled through a combination of the following:

(i) The midgrid bounce-back BC [55] leading to a zero true slip [13]. It is based on the fact [19] that water molecules do not directly slide on solid walls.

(ii) A continuous and exponentially decaying F-S interaction force resulting in a change of fluid viscosity near the solid surface [20] and thus an apparent fluid slip [13] that can be positive or negative. This force function, recognized as an apparent extra attraction [33] responsible for apparent fluid slip (damping), is analogous to the hydrophobic attraction force between solid surfaces [34–36]. Differently from the force function in [15,16], it is established between fluid particles and solid particles at the boundary wall (except inside the solid space), and thus it can be readily extended to porous media (not limited to capillary tubes with flat surfaces).

(iii) The single-phase LBM describing the thermodynamically stable bulk fluid, where the molecular interaction within a liquid is negligible compared with the F-S interaction.

The proposed LBM is detailed in Sec. II. Based on this mesoscopic LBM approach with a validation against a benchmark microchannel flow experiment [5], the effects of interaction parameters on the slip length and the permeability ratio are investigated, and then the permeability ratio considering the slip length is analytically estimated for a capillary tube. The question whether slip length depends on shear rate is also addressed. These investigations are further extended to a porous medium and the importance of F-S interaction to the permeability of microporous media is elucidated. These results are presented and analyzed in Sec. III. The last section draws some conclusions.

II. MESOSCOPIC LBM APPROACH

The LBM on the basis of mesoscopic kinetic theory is not only a modification of the lattice gas model, but also a discretization of the continuous Boltzmann equation [55].

Recently, it has been widely applied for simulations of fluid behaviors including multiphase flows [60] and fluid slip [14–16,56–59].

Within the single-relaxation-time LBM framework, the fluid motion at position $\mathbf{x}$ at time t is described by a set of particle distribution functions f_i related to the ith discrete velocity direction. With the Bhatnagar-Gross-Krook approximation, these distribution functions evolve on the uniform lattice grid according to the following lattice Boltzmann equation [55]:

$$f_i(\mathbf{x}+\mathbf{e}_i\Delta t, t + \Delta t)-f_i(\mathbf{x}, t)= \frac{\Delta t}{\tau}\big[f_i^{\text{eq}}(\mathbf{x}, t) - f_i(\mathbf{x}, t)\big],$$
(1)

where $\boldsymbol{e}_i$ is the discrete velocity, τ the relaxation time, Δt the time step, and $f_i^{\text{eq}}(\mathbf{x}, t)$ the Maxwell-Boltzmann distribution function. The left-hand side is a streaming process, where the particle distribution f_i passes to the neighboring nodes, and the right-hand side is a collision operator, where the particle distribution f_i is partially relaxed to the equilibrium distribution f_i^{eq}.

This discrete velocity model is commonly referred to as the $D_d Q_m$ model, where d and m are the number of dimensionalities and discrete velocities, respectively [55]. The discrete velocities $\boldsymbol{e}_i$ for D_2Q_9 and D_3Q_{19} LBMs are given in Appendix A. To enable D_2Q_9 and D_3Q_{19} LBMs to recover the NS equation, the relaxation time τ is related to the kinematic viscosity ν by $\nu = c_s^2 \Delta t(\tau/\Delta t - 0.5)$ [55], where the sound speed c_s is taken as $c_s^2 = 1/3$. The time step Δt is given by $\Delta t = 1$. The equilibrium distribution function is expressed as [55]

$$f_i^{\text{eq}}(\mathbf{x}, t) = \rho w_i\left[1 + \frac{\mathbf{e}_i \cdot \mathbf{u}^{\text{eq}}}{c_s^2} + \frac{(\mathbf{e}_i \cdot \mathbf{u}^{\text{eq}})^2}{2c_s^4} - \frac{\mathbf{u}^{\text{eq}} \cdot \mathbf{u}^{\text{eq}}}{2c_s^2}\right],$$
(2)

where w_i are the weight coefficients, which are given in Appendix B for D_2Q_9 and D_3Q_{19} LBMs, and $\boldsymbol{u}^{\text{eq}}$ the equilibrium velocity which can be calculated by $\mathbf{u}^{\text{eq}} = \mathbf{u} + \tau\mathbf{F}/\rho$ when the external body force $\mathbf{F}$ is involved [55]. This scheme was proposed by Shan and Chen [61] and thus called the SC force scheme.

The macroscopic fluid density ρ is considered as a series of direction-specific fluid densities, and the macroscopic flow velocity $\mathbf{u}$ is referred to as an average of the microscopic velocities weighted by the directional densities [55]

$$\rho = \sum_i f_i, \quad \mathbf{u} = \frac{1}{\rho}\sum_i f_i\boldsymbol{e}_i.$$
(3)

$\tau = 1$ is the safest value far away from 0.5 to circumvent the numerical instability, and the Mach number has to satisfy $M_a = |\mathbf{u}|_{\text{max}}/c_s \ll 1$ under the incompressible limit [55].

For the steady-state flow, the simulation runs for a sufficient number of time steps until the equilibrium criterion of velocity $\mathbf{u}^n$ is reached. Within a time step $t^{n-1} \to t^n$, the LBM simulation is carried out as follows:

(i) The equilibrium particle distributions $f_i^{\text{eq},\, n-1}$ are calculated from density ρ^{n-1} and velocity $\mathbf{u}^{n-1}$ using Eq. (2), and then the particle distribution functions f_i^{n-1} are collided following the BGK rule in Eq. (1).

(ii) f_i^{n-1} streaming to the neighboring nodes and then BC treatment give f_i^n; the periodic BC is used on the periodic boundary [55]; when the solid walls in the form of zigzag representation are present, f_i^n on the solid nodes are obtained using the midgrid bounce-back BC [55], such as $f_i^n = f_{-i}^n$ (where $-i$th represents the opposite direction to ith); this leads to a zero true slip [13] based on the consideration [19] that water molecules do not directly slide on solid walls.

(iii) Density ρ^n and velocity $\boldsymbol{u}^n$ are computed using f_i^n based on Eq. (3).

A. Explicit force scheme

In the SC force scheme within the aforementioned LBM framework, the momentum transfer due to involvement of external body force is directly incorporated into the equilibrium velocity [61]. The SC force scheme is straightforward, but its numerical results of velocity and density highly depend on the relaxation time when surface force is involved [62]. The inclusion of surface force produces undesirable spurious velocities, which cannot be neglected [63]. To overcome these limitations, another scheme, namely, the explicit-force (EF) scheme proposed by He *et al.* [64], will be used in this paper.

In the EF scheme, a forcing term φ_i accounting for changes in the distribution function due to the external body force $\mathbf{F}$ is defined by [63,64]

$$\varphi_i(\mathbf{x}, t) = \frac{\mathbf{F} \cdot (\mathbf{e}_i - \mathbf{u}^{\text{eq}})}{\rho c_s^2} f_i^{\text{eq}}(\mathbf{x}, t),$$
(4)

where $f_i^{\text{eq}}(\mathbf{x}, t)$ keeps the same form as Eq. (2), but $\mathbf{u}^{\text{eq}}$ is replaced by $\mathbf{u}^{\text{eq}} = \mathbf{u}$. Thus, the momentum substituted into Eq. (2) is different between the SC and EF schemes. In the SC scheme, $\mathbf{u}^{\text{eq}}$ is an effective momentum plus the changes in momentum due to $\mathbf{F}$; meanwhile, in the EF scheme, $\mathbf{F}$ is directly introduced into the distribution function f_i, and $\mathbf{u}^{\text{eq}}$ is simply an effective momentum.

The forcing term φ_i is directly incorporated into the lattice Boltzmann equation in Eq. (1) with the collision operator unchanged, resulting in an implicit expression [63,64]

$$\begin{aligned}f_i(\mathbf{x} + \mathbf{e}_i\Delta t, t + \Delta t) &- f_i(\mathbf{x}, t)\\ &= \frac{\Delta t}{\tau}\big[f_i^{\text{eq}}(\mathbf{x}, t) - f_i(\mathbf{x}, t)\big]\\ &+ \frac{\Delta t}{2}[\varphi_i(\mathbf{x} + \mathbf{e}_i\Delta t, t + \Delta t) + \varphi_i(\mathbf{x}, t)].\end{aligned}$$
(5)

Here a transformation $h_i(\mathbf{x}, t) = f_i(\mathbf{x}, t) - \frac{\Delta t}{2}\varphi_i(\mathbf{x}, t)$ is applied to Eq. (5) yielding the following explicit expression [63,64]:

$$\begin{aligned}h_i(\mathbf{x} + \boldsymbol{e}_i\Delta t, t + \Delta t) &- h_i(\mathbf{x}, t)\\ &= \frac{\Delta t}{\tau}\left[f_i^{\text{eq}}(\mathbf{x}, t) - h_i(\mathbf{x}, t) - \frac{\Delta t}{2}\varphi_i(\mathbf{x}, t)\right] + \Delta t\varphi_i(\mathbf{x}, t).\end{aligned}$$
(6)

Then the macroscopic fluid density ρ and flow velocity $\mathbf{u}$, which are different from Eq. (3), are defined by [63,64]

$$\rho = \sum_i h_i; \quad \mathbf{u} = \frac{1}{\rho}\left(\sum_i h_i\mathbf{e}_i + \frac{\Delta t}{2}\mathbf{F}\right).$$
(7)

B. Multiple-relaxation-time scheme

Here a multiple-relaxation-time (MRT) scheme is also provided in combination with the EF scheme to alleviate the dependency of numerical results on relaxation time. In the MRT formulation, the lattice Boltzmann equation with a collision operator different from that in Eq. (5) is given by an implicit expression [63]

$$
\begin{aligned}
f_i(\mathbf{x} + \mathbf{e}_i \Delta t, & t + \Delta t) - f_i(\mathbf{x}, t) \\
&= \mathbf{M}^{-1}\mathbf{SM}\big[f_i^{\text{eq}}(\mathbf{x}, t) - f_i(\mathbf{x}, t)\big] \\
&+ \frac{\Delta t}{2}[\varphi_i(\mathbf{x} + \mathbf{e}_i \Delta t, t + \Delta t) + \varphi_i(\mathbf{x}, t)].
\end{aligned} \tag{8}
$$

When the definition of $h_i(\mathbf{x}, t)$ is introduced, Eq. (8) is transformed into the following explicit form [63]:

$$
\begin{aligned}
h_i(\mathbf{x} + \boldsymbol{e}_i \Delta t, & t + \Delta t) - h_i(\mathbf{x}, t) \\
&= \mathbf{M}^{-1}\mathbf{SM}\bigg[f_i^{\text{eq}}(\mathbf{x}, t) - h_i(\mathbf{x}, t) - \frac{\Delta t}{2}\varphi_i(\mathbf{x}, t)\bigg] \\
&+ \Delta t \varphi_i(\mathbf{x}, t),
\end{aligned} \tag{9}
$$

where $\mathbf{M}$ is a transformation matrix, and $\mathbf{S}$ a diagonal relaxation matrix. For the D_2Q_9 LBM, the transformation matrix $\mathbf{M}$ is given by [63]

$$
\mathbf{M} = \begin{bmatrix}
1 & 1 & 1 & 1 & 1 & 1 & 1 & 1 & 1 \\
-4 & -1 & -1 & -1 & -1 & 2 & 2 & 2 & 2 \\
4 & -2 & -2 & -2 & -2 & 1 & 1 & 1 & 1 \\
0 & 1 & 0 & -1 & 0 & 1 & -1 & -1 & 1 \\
0 & -2 & 0 & 2 & 0 & 1 & -1 & -1 & 1 \\
0 & 0 & 1 & 0 & -1 & 1 & 1 & -1 & -1 \\
0 & 0 & -2 & 0 & 2 & 1 & 1 & -1 & -1 \\
0 & 1 & -1 & 1 & -1 & 0 & 0 & 0 & 0 \\
0 & 0 & 0 & 0 & 0 & 1 & -1 & 1 & -1
\end{bmatrix} \tag{10}
$$

and the diagonal relaxation matrix is given by [63]

$$
\mathbf{S} = \text{diag}[s_c,\ s_e,\ s_\varepsilon,\ s_c,\ s_q,\ s_c,\ s_q,\ s_v, s_v], \tag{11}
$$

where s_i is the relaxation rate of h_i in each discrete velocity direction. If all s_i in Eq. (10) are set as $s_i = 1/\tau$, the MRT formulation in Eq. (9) is reduced to Eq. (6). The relaxation parameters $s_e, s_\varepsilon, s_v, s_q$ are free parameters and correspond to the nonconserved moments, such as energy, energy squared, energy flux, and stress tensor, respectively [63]. In this work, they are defined by $s_e = s_\varepsilon = s_v = 1/\tau$ and $s_q = 8(2\tau - 1)/(8\tau - 1)$ [65]. The relaxation parameter s_c has a nonzero value and corresponds to the conserved moments, such as density and momentum [63]. When $s_c = 1$, $\mathbf{u}^{\text{eq}}$ can be derived as $\mathbf{u}^{\text{eq}} = \mathbf{u}$ to guarantee that the MRT scheme combined with EF scheme conserves momentum [63]. Furthermore, Eqs. (10) and (11) can be easily extended to the D_3Q_{19} LBM [63]. The macroscopic fluid density ρ and flow velocity $\mathbf{u}$ keep the same as Eq. (7).

C. Fluid-solid interaction

The F-S interaction may be a more reliable index of hydrophobicity of a solid surface than wettability [11–16,26–31].

It is a long-range surface force, a few orders of magnitude larger than the van der Waals attraction, and has been recognized as an extra attraction [33] responsible for an apparent fluid slip but without a theoretical formulation [32,33]. Thus we propose a continuous and exponentially decaying F-S interaction force resulting in a change of fluid viscosity near the solid surface [20] and thus an apparent slip [13] based on an analogy to the hydrophobic attraction force between solid surfaces [34–36],

$$
\mathbf{F}_w = -\rho g_w \exp\bigg(-\frac{\|\mathbf{x} - \mathbf{x}_w\|}{\eta}\bigg)\mathbf{e}, \tag{12}
$$

where $\mathbf{x}_w$ is the position of an ensemble of solid particles at the boundary wall (except inside the solid space), from which the unit vector for the direction $\mathbf{e} = (\mathbf{x} - \mathbf{x}_w)/\|\mathbf{x} - \mathbf{x}_w\|$ points to the fluid particles, g_w is the interaction strength, and η is the decay length. The following should be noted:

(i) $\mathbf{F}_w$ is applied to fluid particles.

(ii) Equation (12) is different from the fluid–solid wall interaction force function [15,16], because it is established between fluid particles and solid particles at the boundary wall, as illustrated by the inclusion of unit vector $\mathbf{e}$, and thus can be readily extended to porous media.

(iii) Equation (12), with two free parameters, such as g_w and η, allows the simulation of profiles of density and velocity near the solid surface with a high accuracy.

(iv) Equation (12) is applied here to the situation where the thermodynamically stable bulk fluid is governed by a single-phase LBM, and thus is not related to contact angle.

The roles of the two free parameters, g_w and η, in the interaction force are illustrated in Fig. 1(a), and the link between the F-S interaction and the flow behavior is presented in Fig. 1(b). g_w determines an effective strength of the F-S interaction which can be positive or negative. When $g_w > 0$ ($g_w < 0$), the F-S interaction force is repulsive (attractive) [Fig. 1(a)], which leads to a fluid slip (damping), occurring not directly on solid surfaces [19] but over a depleted (condensed) layer [20]. The fluid slip (damping) is the so-called apparent phenomenon [Fig. 1(b)], because the extrapolated Poiseuille-type bulk velocity vanishes outside (inside) the solid wall, even if the actual near-wall velocity does vanish exactly at the wall. To quantify the amount of apparent fluid slip (damping), the slip length λ is defined as the distance between the apparent solid plane where the bulk velocity extrapolates to zero in the presence of F-S interaction and the real solid plane where the velocity is actually zero under the no-slip condition. Also, the permeability ratio k/k^* is defined here as a ratio of apparent permeability k in the presence of F-S interaction to intrinsic permeability k^* under the no-slip condition. Therefore, for the fluid slip (damping) where $g_w > 0$ ($g_w < 0$), the apparent no-slip plane lies within the solid (fluid) resulting in a positive (negative) slip length, i.e., $\lambda > 0$ ($\lambda < 0$), and then the permeability of a capillary tube or a porous medium increases (decreases) with the ratio of $k/k^* > 1$ ($k/k^* < 1$).

Meanwhile, η controls the effective distance of F-S interaction [Fig. 1(a)], which is defined here as the distance from the solid surface with the maximum strength to where the magnitude of F_w/ρ decays to 1% of its maximum. Thus, the effective interaction distance is 4.0 (6.0) lattice units if
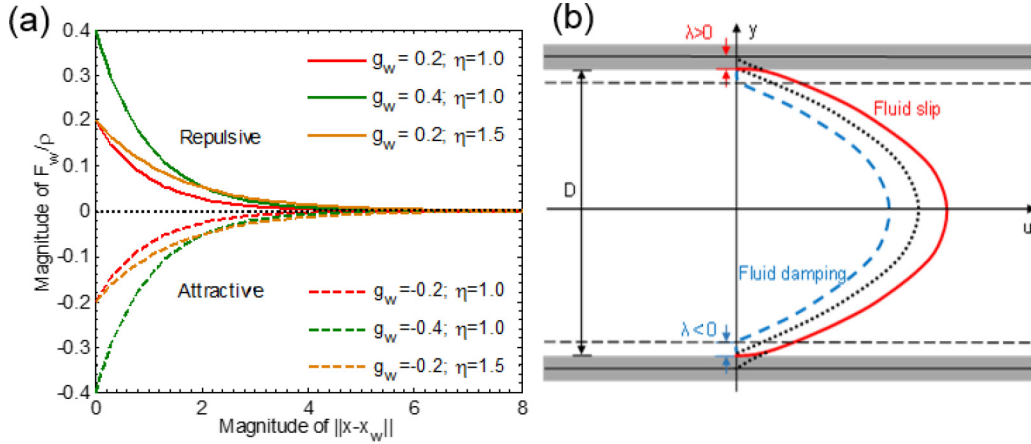
FIG. 1. (a) Typical forces of fluid-solid interaction as a function of distance. All the variables are presented in lattice units, and the same in the following figures unless stated otherwise. (b) Velocity profile and slip length of fluid slip (damping) due to repulsive (attractive) interactions. In panel (b), the dotted line represents the velocity profile in the absence of F-S interaction.

$\eta = 1.0$ (1.5) is taken, and it varies proportionally to the value of η. An increase in $|g_w|$ and (or) η leads to a stronger F-S interaction. One lattice unit is proposed to be 25 nm in the LBM approach, and then the effective interaction distance equals 100 nm for $\eta = 1.0$, which agrees with the observed decaying force curve [32–36]. Moreover, if water ($\rho = 1.0$ g/cm^3, $\nu = 1.5 \times 10^{-6}$ m^2/s) is considered as the lattice fluid ($\rho_0 = 1.0$, $\nu = 0.15$), the force strength can be converted to $F_w = 0.002$ dyn/cm^3 near the solid wall for $g_w = 0.2$, the order of magnitude of which is consistent with that in the simulation [57].

Not only an interaction force $\mathbf{F}_w$ is exerted on the fluid by the solid particles, but also an external body force $\mathbf{F}_g = \rho \mathbf{g}$ ($\mathbf{g}$ is an acceleration of the body force) as the flow driver, due to its easy implementation in the LBM simulation. Thus, the total force $\mathbf{F}$ acting on the fluid particles is $\mathbf{F} = \mathbf{F}_w + \mathbf{F}_g$ which arises in Eq. (4) in the numerical implementations. Integrating the interaction force at the particle level is specific to the solid surface area, and thus the dimensionless number, the ratio of total interaction force to body force (g), can be expressed by

$$\frac{\mathbf{F}_w \times \text{Specific solid surface area}}{\mathbf{F}_g} = \frac{|g_w|}{g D_c}, \qquad (13)$$

where D_c is the characteristic length of the flow channel. Another dimensionless number describing the flow pattern is the Reynolds number, the ratio of inertial force to viscous force, which is given by [17,18]

$$R_e = \frac{u_c D_c}{\nu}, \qquad (14)$$

where u_c is the characteristic velocity of the flow system.

III. RESULTS AND ANALYSIS

In this section, the mesoscopic F-S interaction force function will be first validated against a benchmark microchannel flow experiment [5] using only the EF force scheme, and then applied to the flows in a capillary tube and through a porous medium using both the EF and MRT force schemes.

A. Model validation

Tretheway and Meinhart [5] measured the velocity profiles of deionized water flow in a three-dimensional microchannel. The clean glass surface is naturally hydrophilic, but it becomes hydrophobic when coated with a hydrophobic OTS (in full, octadecyltrichlorosilane) layer at the wall. In the LBM approach, the hydrophilic or hydrophobic surface is realized by the attractive or repulsive F-S interaction. As shown in Fig. 2, the directions of length, width, and depth of the channel are denoted as the x, y, and z coordinates, respectively. The microchannel has a length of 8.25 cm, along which the water flow can fully develop over a cross section of 300 μm $\times$ 30 μm [5]. Four solid walls in the flow direction are uniformly hydrophilic or hydrophobic. Deionized water is injected into the microchannel at a constant volume flux of 200 ml/h using a syringe pump [5]. Velocity measurements using micron-particle image velocimetry (μ-PIV) are made in the middle plane of the channel (15 μm from the top) and within 25 μm near the wall where the free-stream velocity can be almost achieved (Fig. 2) [5]. In the LBM simulation, the channel length is shortened to 30 μm (Fig. 2), which can be justified by the periodic BC used in the flow direction. Thus, the dimension of computaional domain is 30 μm $\times$ 300 μm $\times$ 30 μm in the x, y, and z directions, respectively.
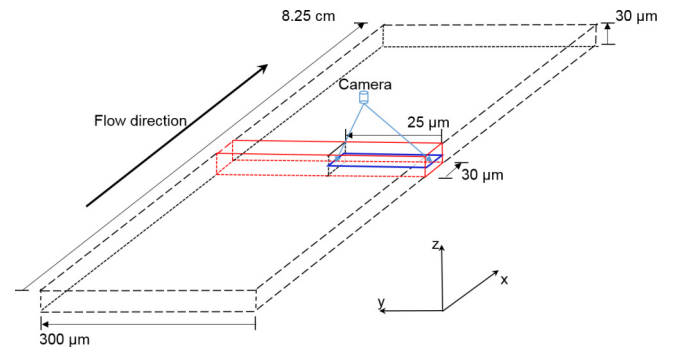

FIG. 2. Dimension of a three-dimensional microchannel in Tretheway and Meinhart's experiment [5] and in the LBM simulation (red lines).
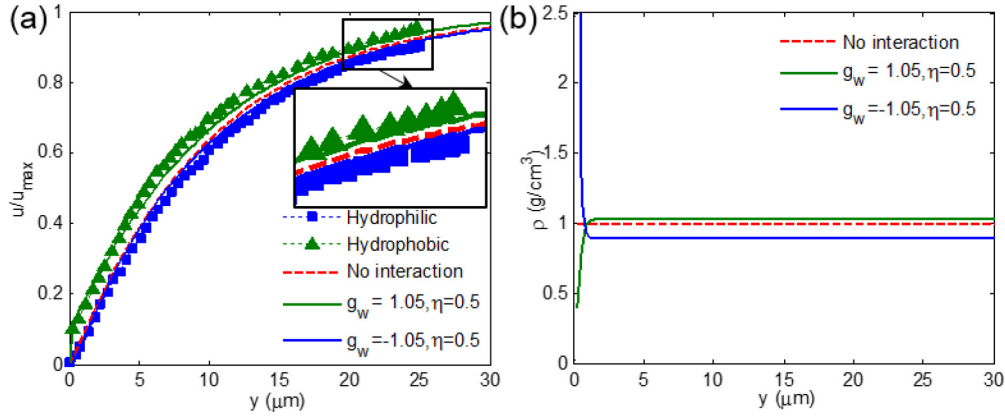
FIG. 3. Spanwise profiles of normalized velocity (a) and water density (b) in Tretheway and Meinhart's experiment [5] (squares and triangles) and in the LBM simulation. In panel (a), the slight difference between various velocity profiles is highlighted in a square.

$\eta = 0.5$ was taken to ensure that at least two lattice layers are involved in the F-S interaction (the effective interaction distance is 2 lattice units). To reach a compromise between the physics of molecular interaction and the computational efforts, one lattice unit is taken to be 300 nm here, and thus the physical interaction distance is 600 nm, which is somewhat exaggerated [32–36] but results in an acceptable lattice grid of $100 \times 1000 \times 100$. The flowing water ($\rho = 1.0$ g/cm^3, $\nu = 1.5 \times 10^{-6}$ m^2/s) can be converted to a lattice fluid of $\rho_0 = 2.7$ and $\nu = 0.5$. The magnitude of body force in the flow direction is adjusted to attain the specified average flow rate of 0.0062 m/s [5]. The steady-state velocity field is reached within 8.0×10^4 time steps, and the simulated velocity profiles are taken from the same plane as the measured ones for comparison.

Figure 3(a) illustrates the measured and simulated velocity profiles (normalized by the free-stream velocity) on hydrophilic and hydrophobic solid walls. There is a slight but distinguishable drop in the measured profile on the hydrophilic surface, compared with the simulated profile under the no-slip condition (no F-S interaction), where $g = 4.113 \times 10^{-7}$ is used to recover the given average flow rate. This finding, which was also obtained in Zhu *et al.*'s simulation [57], seems to violate the no-slip boundary assumed on the hydrophilic surface. Instead, it means that more than one water layer are adsorbed (immobilized) at the wall due to the F-S interaction. This phenomenon is called as the multilayer sticking [13]. The hydrophilic velocity profile can be better matched by a simulation with $g = 4.3 \times 10^{-7}$ and $g_w = -1.05$, where an attractive F-S interaction is involved, and confirms the existence of a negative slip length [26–28]. For the hydrophobic solid surface, the slip velocity at the wall reaches about 10% of the free-stream velocity and yields a slip length of around 1 μm [5]. The simulation with $g = 3.6 \times 10^{-7}$ and $g_w = 1.05$ reasonably recovers the slip velocity and the hydrophobic velocity profile, making it plausible that the fluid slip is due to the repulsive interaction at the F-S interfaces.

Figure 3(b) presents the water density profiles near the hydrophobic and hydrophilic solid walls with the interaction parameters used for the measured velocity profiles. When the

interaction is repulsive, water molecules are expelled from solid surfaces and the water density in a very thin layer decreases significantly. Such a decrease results in a decrease of shear viscosity and thus the liquid slippage behavior. It is consistent with Derjaguin and Churaev's finding [20] that the slip is attributed to the depleted water region or a vapor layer near the hydrophobic surface. On the contrary, the attractive interaction makes water molecules to gather near the solid surface and results in an increase of water shear viscosity and then the fluid damping behavior. The thickness of the depleted (condensed) water region of about 1–2 μm is somewhat exaggerated due to the limitation in the grid resolution, which is not the focus of interest in our work. Overall, these results suggest that the proposed F-S interaction force within the LBM framework is sound, as it can recover the fluid slip (damping) behavior, and also is able to provide insights into the underlying mechanism.

B. Flow in a capillary tube

The fluid flow in a thin capillary tube as shown in Fig. 1(b) is the so-called Poiseuille-type flow, where the velocity reaches zero at the wall and the maximum in the middle. Under the no-slip condition, the velocity profile in a two-dimensional tube is a parabolic curve given by [17,18]

$$u(y) = \frac{g}{2\nu} y(D - y), \quad (15)$$

where y is the coordinate in the spanwise direction, and D the tube diameter. In the LBM simulation, the tube wall is defined as the solid boundary, and the inlet and outlet of the tube are treated as the periodic boundary [Fig. 1(b)].

1. Slip length

When the tube wall is hydrophobic or hydrophilic, the fluid slip (damping) behavior is considered by introducing the slip length λ into the velocity profile [Fig. 1(b)], as follows:

$$u'(y) = \frac{g}{2\nu'} (y + \lambda)(D + \lambda - y), \quad (16)$$

where u' is the spanwise velocity of bulk fluid, and ν' the kinematic viscosity of bulk fluid in the presence of the F-S
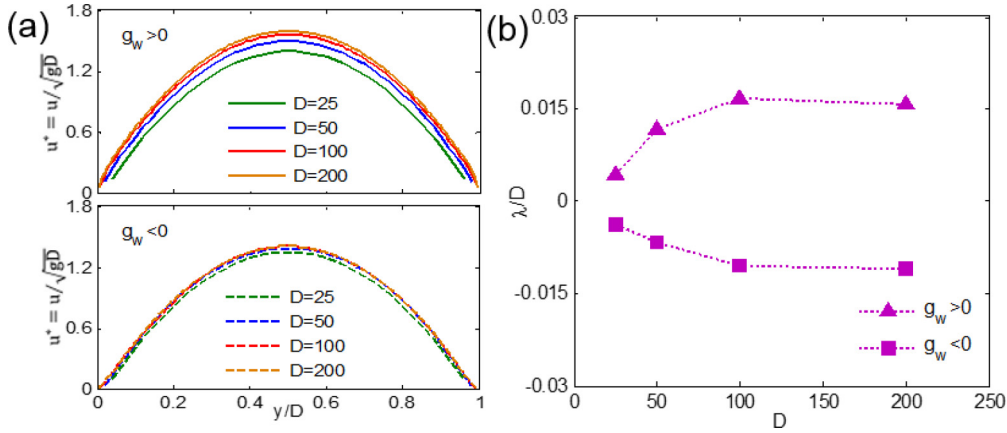
FIG. 4. Spanwise profiles of normalized velocity (a), and normalized slip length with respect to the lattice resolution (b). In the case of $D = 100$, $g = 3.2 \times 10^{-6}$, $g_w = \pm 0.2$, and $\eta = 1.0$ are taken.

interaction. λ is the same at two parallel walls. It is noted that Eq. (16) is only an approximation to the bulk flow velocity before it is justified by the simulations. No analytical description of the near-wall flow velocity is available. In our analysis, the bulk flow region is defined as $10 < y < D - 10$ in the spanwise direction. By fitting the simulated bulk velocity profiles to Eq. (16) based on the regression analysis, the values of kinematic viscosity ν' and slip length λ can be obtained simultaneously. When calculating the value of λ, the nonphysical slip length of -0.5 caused by the midgrid bounce-back BC [14,55] has to be excluded.

The lattice resolution effect on the slip length, as an important aspect of the LBM simulation, is investigated. Maintaining $\nu = 0.15$, when the lattice number D is varied, the dimensionless numbers in Eqs. (13) and (14) and η/D have to be fixed to keep the same physical flow system. Here the characteristic length D_c and velocity u_c can be represented by the diameter D and the midchannel velocity $u_{\max} = g D^2 / 8\nu$, respectively. In this way, it is interesting to note that the product of the two dimensionless numbers in Eqs. (13) and (14), $|g_w| D^2 / 8\nu^2$, combined with $\eta \propto D$ and the fixed ν, gives a new dimensionless number, $|g_w| \eta^2$. In Fig. 4(a), the neighboring normalized velocity profiles are shown to be closer as D increases, and the ratio of the L_2 norm deviations between neighboring profiles, i.e., $\|u^*|_{D=25} - u^*|_{D=50}\| : \|u^*|_{D=50} - u^*|_{D=100}\| : \|u^*|_{D=100} - u^*|_{D=200}\|$, are $3.26 : 1.86 : 1.00$ ($3.70 : 1.97 : 1.00$) for $g_w > 0$ ($g_w < 0$). In Fig. 4(b), the normalized slip length tends to be convergent as D increases, and there is not much difference between $D = 100$ and $D = 200$. Thus, the proposed LBM model is validated to be convergent and the simulation results tend to be lattice resolution independent as $D \geqslant 100$.

Table I lists the fitted values of ν' and λ for the interaction parameters $g_w = \pm 0.2$, $\eta = 1.0$ with respect to different magnitudes of body force g, tube diameters D, and kinematic viscosities ν. The tube length is always $2D$. All the regression results show that the simulated bulk velocity profiles follow the approximation given by Eq. (16) and thus keep the parabolic nature as that expressed by Eq. (15) under the no-slip condition; the relative deviations between the fitted ν' and the exact ν are small, within 0.16%, indicating that the

bulk fluid property is not affected by the molecular interaction at the F-S interface. The main change due to the F-S interaction is the inclusion of the slip length λ into the bulk velocity profile as presented by Eq. (16). In other words, the bulk flow in the presence of the F-S interaction resulting in a slip length of λ is equivalent to that in a tube with a diameter of $(D + 2\lambda)$ predicted under the no-slip condition.

Another interesting observation from Table I is that for g ranging from 2.0×10^{-6} to 1.0×10^{-5}, D varying from 100 to 200, and ν between 0.05 and 1.5, the fitted λ values change slightly and the relative deviations between each other are within 1.98%, 7.31%, and 4.44%, respectively. It appears that the slip length is constant with the varied values of g, D, and ν. The shear rate at the wall ($y = 0$) can be derived, such as $\frac{\partial u}{\partial y} = \frac{gD}{2\nu}$, and we note that g, D, and ν are the constituents of shear rate. This leads to an important finding that slip length is independent of shear rate in our work. In fact, a consensus on whether slip length is dependent on shear rate has not been reached in previous studies. On one hand, the slip length observed on the smooth hydrophobic surface is irrelevant to shear rate up to 5000 s^{-1} [10], and the slip length measured on an OTS surface is 400 nm $\pm$ 100 nm for shear rates between 200 s^{-1} and 2000 s^{-1} [29]. On the other hand, the onset of slip occurs only when a critical velocity (proportional to shear rate) is exceeded, and the amount of slip depends strongly on velocity [8]. The slip length is nearly constant at low shear rates, and then increases rapidly with shear rate beyond a critical level [27]. The slip dependence on the velocity (shear rate) may be due to that shear induces the growth of bubbles over which the liquid flows [20–22]. The slip independence of g and D has important implications for the permeability of a porous medium passing a fluid: (1) the increased pressure gradient (equivalent to body force) cannot drive the immobilized liquid near the wall and thus cannot improve the permeability, which is contrary to Liu *et al.*'s observations [43]; (2) for the thin capillary tube or the microporous medium, the nearly constant slip length leads to an increase in the ratio of slip length to flow channel size ($|\lambda|/D$), resulting in a more profound effect of fluid slip on the permeability.

Figure 5(a) displays the simulated spanwise velocity profiles with respect to strength parameters, g_w and η for $D =$

TABLE I. Comparison of exact ν and fitted ν', and dependencies of λ on g for $D = 100$, $\nu = 0.15$, on D for $g = 5.0 \times 10^{-6}$, $\nu = 0.15$, and on ν for $g = 5.0 \times 10^{-6}$, $D = 100$. All the variables are presented in lattice units, and the same in the following tables unless stated otherwise.

| Cases | $g_w = 0.2, \eta = 1.0$ | | | | $g_w = -0.2, \eta = 1.0$ | | | |
	Fitted ν'	Relative deviation	Fitted λ	Relative deviation	Fitted ν'	Relative deviation	Fitted λ	Relative deviation
$g = 2.0 \times 10^{-6}$	0.1502	0.133%	1.7042		0.1499	−0.067%	−0.9699	
4.0×10^{-6}	0.1498	−0.133%	1.6763	−1.64%	0.1500	0.000%	−0.9617	−0.85%
6.0×10^{-6}	0.1500	0.000%	1.7219	1.04%	0.1499	−0.067%	−0.9891	*1.98%*
8.0×10^{-6}	0.1499	−0.067%	1.7091	0.29%	0.1500	0.000%	−0.9817	1.22%
1.0×10^{-5}	0.1500	0.000%	1.7279	1.39%	0.1501	0.067%	−0.9693	0.06%
$D = 100$	0.1499	−0.067%	1.6938		0.1499	−0.067%	−0.9771	
125	0.1501	0.067%	1.7483	3.22%	0.1500	0.000%	−0.9728	−0.44%
150	0.1500	0.000%	1.7881	5.57%	0.1500	0.000%	−1.0007	2.42%
175	0.1500	0.000%	1.8031	6.45%	0.1500	0.000%	−1.0063	2.99%
200	0.1502	0.133%	1.8176	*7.31%*	0.1501	0.067%	−1.0068	3.04%
$\nu = 0.05$	0.0500	0.000%	1.7225		0.0500	0.000%	−0.9664	
0.15	0.1501	0.067%	1.7358	0.77%	0.1501	0.067%	−0.9654	−0.10%
0.5	0.5001	0.020%	1.7168	−0.33%	0.4999	−0.020%	−0.9860	2.03%
1.0	0.9995	−0.050%	1.6772	−2.63%	0.9984	*−0.160%*	−1.0093	*4.44%*
1.5	1.4988	−0.080%	1.7024	−1.17%	1.4993	−0.047%	−0.9848	1.90%

100. The bulk velocity profiles ($10 < y < D - 10$) keep the parabolic shape in all the simulations, irrespective of the presence of the F-S interaction. The maximum velocity (u_{max}) in the middle for $g_w > 0$ ($g_w < 0$) is larger (smaller) than

that for $g_w = 0$, and the increase (decrease) of u_{max} is nonlinear with $|g_w|$ and η. The velocity decreases to zero much faster (slower) for $g_w > 0$ ($g_w < 0$) than that for $g_w = 0$ as approaching the tube wall. At the same magnitude of $|g_w|$ and
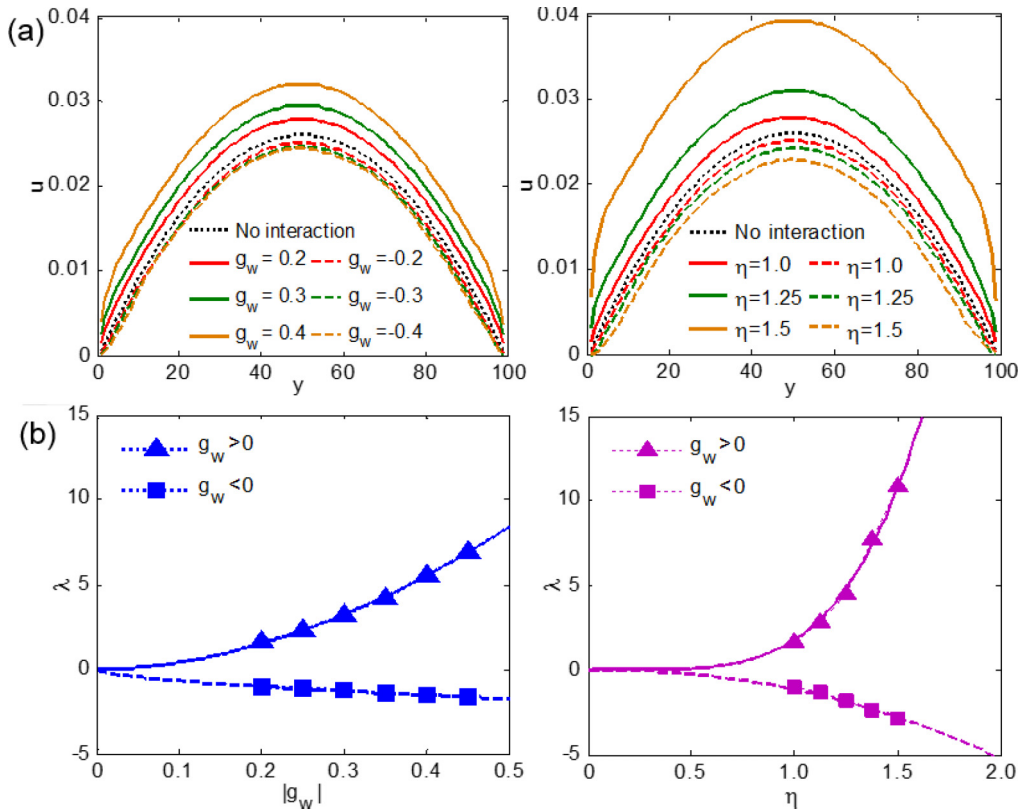

FIG. 5. Spanwise velocity profiles with respect to g_w for $\eta = 1.0$ and with respect to η for $g_w = \pm 0.2$ (a), and dependencies of slip length on g_w for $\eta = 1.0$ and on η for $g_w = \pm 0.2$ (b). In panel (b), triangles and squares represent the simulated data for $g_w > 0$ and $g_w < 0$, respectively; solid and dashed curves are the fitted curves for $g_w > 0$ and $g_w < 0$, respectively.

TABLE II. Coefficients for fitted λ in Eq. (17).

Cases		a_0	a_1	a_2	Relative deviation from $a_2 = 2a_1 + 1$
Capillary tube	$g_w > 0$	28.63	1.797	4.774	3.92%
	$g_w < 0$	−2.614	0.586	2.628	20.9%
Porous media	$g_w > 0$	6.857	1.262	3.427	−2.75%
	$g_w < 0$	−2.335	0.851	2.867	6.11%

TABLE III. Coefficients for fitted k/k^* in Eq. (20).

Cases		b_0	b_1	b_2	Relative deviation from $b_2 = 2b_1 + 1$
Capillary tube	$g_w > 0$	1.699	1.757	4.725	4.67%
	$g_w < 0$	−0.186	0.733	2.500	1.38%
Porous media	$g_w > 0$	0.503	1.315	3.416	−5.90%
	$g_w < 0$	−0.160	0.791	2.423	−6.16%

η, the variation of $u_{\max}$ is always more significant for $g_w > 0$ than that for $g_w < 0$.

As described in Fig. 5(b), the simulated slip length varies with $|g_w|$ and η nonlinearly, and changes more dramatically for $g_w > 0$ than for $g_w < 0$. These nonlinear increasing trends of slip length can be expressed by a power law function

$$\lambda = a_0 |g_w|^{a_1} \eta^{a_2}, \qquad (17)$$

where a_0 is the fitted proportionality, and a_1 and a_2 the fitted exponents for $|g_w|$ and η, respectively. The slip length fitted by Eq. (17) can naturally go back to zero, when the interaction strength is zero ($|g_w| = 0$ or $\eta = 0$). The fitted values of a_i are listed in Table II, and they can explain all the qualitative features of the increasing trend. In particular, the slip length increases with $|g_w|$, with an exponent less than 1 for $g_w < 0$.

It is noted that as the F-S interaction strengthens and the density gradient becomes steep, the proposed LBM tends to be less stable [66]. But the stability issue is not the focus of interest in our work. The simulated results shown in Figs. 5(a) and 5(b) are within the capability of the LBM used. The maximum (minimum) ratio of slip length to tube diameter, $|\lambda|/D$, that our LBM approach can attain is around 0.10 (0.03) for $g_w > 0$ ($g_w < 0$).

2. Effect on permeability

The influence of F-S interaction on the average flow rate and the tube permeability is also investigated. Despite the density profile in the spanwise direction caused by the interaction as shown in Fig. 3(b), the thickness of the depleted (condensed) water region somewhat exaggerated by the LBM is negligible relative to the flow channel size. Thus the average flow rate can be reasonably expressed by the total volume flux divided by the area of the cross section.

According to the velocity field (u_{ij}) exported by Eq. (7) within the LBM framework, the average flow rate (q) is calculated here by the sum of flow velocities u_{ij} divided by the volume over the entire domain with a size of $M \times N$, i.e.,

$$q = \frac{1}{M \times N} \sum_{ij} (u_{ij}). \qquad (18)$$

It is noted that Eq. (18) is valid irrespective of the presence of the F-S interaction. The permeability ratio, k/k^*, quantifying the permeability variation can be calculated by the ratio of average flow rate (q_{slip}) in the presence of the F-S interaction to that ($q_{\text{no slip}}$) under the no-slip condition with the same driven force, i.e.,

$$\frac{k}{k^*} = \frac{q_{\text{slip}}}{q_{\text{no slip}}}. \qquad (19)$$

Figure 6(a) shows the average flow rate versus the magnitude of body force with respect to strength parameters, g_w and η. All the simulated values of average flow rate are proportional to the body force (zero body force intercept) for Reynolds numbers ($R_e = q_{\text{no slip}} D/\nu$) down to 1.80, as confirmed by the regression analysis. If the body force decreases further, the rising ratio of $|g_w|/g$ (strengthened F-S interaction) will lead to a numerical instability. In terms of the slope of the simulated data, the tube permeability for $g_w > 0$ ($g_w < 0$) is larger (smaller) than that for $g_w = 0$, and changes nonlinearly with g_w and η in a similar way. The absence of a body force intercept agrees with the observation that there is only a change in the slope for the hydrophobic quartz capillaries [3] and the nonaqueous phase liquid (NAPL) wetted fractures [40]. Also, it is consistent with the independence of slip length (and then the effective channel size) on body force observed in our work. Thus, the phenomena of pre-Darcy effect (more than proportional increase) [48–50] and threshold pressure gradient [51–53] observed in shale and clay cannot be recovered by our proposed LBM.

These observations can be demonstrated by the permeability ratio in Fig. 6(b). The variation of k/k^* with $|g_w|$ and η can be fitted by a power law function

$$\frac{k}{k^*} = 1 + b_0 |g_w|^{b_1} \eta^{b_2}, \qquad (20)$$

where b_0 is the fitted proportionality; b_1 and b_2 are the fitted exponents for $|g_w|$ and η, respectively. It is advantageous that the fitted k/k^* in Eq. (20) can be normalized to 1 under the no-slip condition. The values of b_i as listed in Table III can be inherently linked with the variation of simulated data in Fig. 6(b). $b_0 > 0$ ($b_0 < 0$) for $g_w > 0$ ($g_w < 0$) indicates $k/k^* > 1$ ($k/k^* < 1$) for the fluid slip (damping) behavior. When $g_w > 0$, $b_2 > b_1 > 1$ suggests the fast increase (more than being proportional) of k/k^* with $|g_w|$ and η; when $g_w < 0$, $b_2 > 1 > b_1$ implies the slow increase (less than being proportional) with $|g_w|$ but fast increase (more than being proportional) with η. Both b_1 and b_2, which are larger for $g_w > 0$ than those for $g_w < 0$, indicate a stronger effect of repulsive interaction than that of attractive interaction at the same magnitude of strength parameters. The maximum permeability ratio achieved by the LBM model reaches about 1.7, comparable to that measured in a quartz capillary [3] but far less than that observed in a carbon nanotube [4].

By analyzing the exponents of $|g_w|$ and η for the fitted slip length and permeability ratio in Tables II and III, the data of (a_1, a_2) and (b_1, b_2) reasonably follow the same relationship, $y = 2x + 1$, with the relative deviations smaller than 4.67%, except for (a_1, a_2) for $g_w < 0$, which displays a
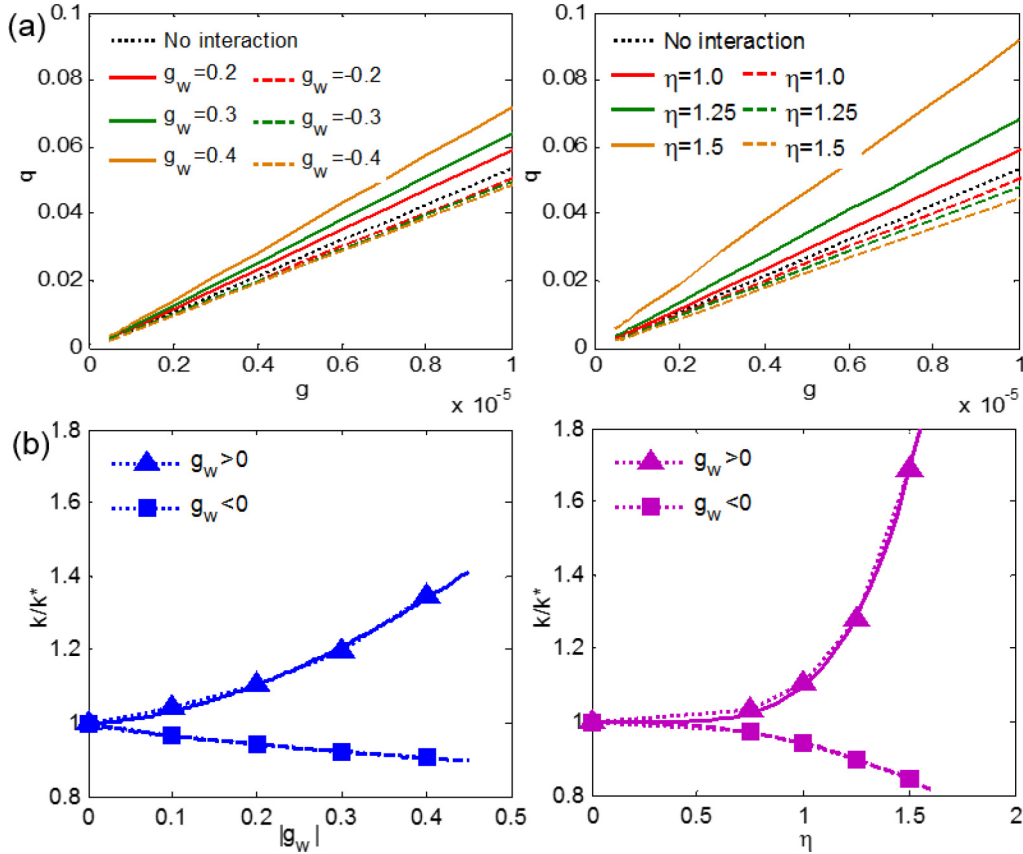
FIG. 6. Average flow rate as a function of g with respect to g_w for $\eta = 1.0$ and with respect to η for $g_w = \pm 0.2$ (a), and dependencies of k/k^* on g_w for $\eta = 1.0$ and on η for $g_w = \pm 0.2$ (b). In panel (b), triangles and squares represent the simulated data for $g_w > 0$ and $g_w < 0$, respectively; solid and dashed curves are the fitted curves for $g_w > 0$ and $g_w < 0$, respectively.

relative deviation as large as 20.9%. The similar effects of $|g_w|$ and η on velocity profile, slip length, and average flow rate versus magnitude of body force and permeability ratio are also evident in Figs. 5 and 6. It can be inferred from these results that the two free strength parameters, $|g_w|$ and η, perhaps can be combined into a simple parameter.

Apart from the simulated and fitted permeability ratios, k/k^* can also be estimated analytically based on the approximated velocity profile given by Eq. (16). As confirmed by the regression results, Eq. (16) can describe the bulk velocity profile well. Equation (16) extrapolated to the solid wall gives a positive (negative) slip velocity for $g_w > 0$ ($g_w < 0$), and thus overestimates (underestimates) the near-wall velocity as well as the average flow rate, compared with the simulated ones. Nevertheless, if the ratio of $|\lambda|/D$ is less than 1, for example, $|\lambda|/D < 1/4$, the overestimation of the F-S interaction effect on permeability can be controlled. Integrating Eq. (16) over the spanwise direction gives the volume flux in the presence of F-S interaction. Based on the validated $v' = v$, the permeability ratio k/k^* considering slip length can be estimated by

$$\frac{k}{k^*} = \frac{\int_0^D \mathrm{u}'(y)dy}{\int_0^D \mathrm{u}(y)dy} = \begin{cases} 1 + \frac{6(D\lambda + \lambda^2)}{D^2}, & \lambda > 0, \\ \left(1 + \frac{2\lambda}{D}\right)^3, & \lambda < 0. \end{cases} \quad (21)$$

With the simulated data of λ in Fig. 5(b), the estimated k/k^* based on Eq. (21) is found to be reasonably consistent with the simulated k/k^* plotted in Fig. 6(b), as shown in Fig. 7(a). Therefore, Eq. (21) offers a robust way for estimating the permeability variation due to the F-S interaction when combined with Eq. (17). As $|\lambda|/D$ increases to no more than 1/4 due to a reduction in the tube diameter D, Eq. (21) can also be used to investigate the effect of tube diameter on permeability ratio for the given strength parameters, as demonstrated in Fig. 7(b). k/k^* increases (decreases) with D for $g_w > 0$ ($g_w < 0$), suggesting that the F-S interaction effect on permeability is crucially important for the thin capillary tubes. When $|\lambda|/D$ approaches 1/4, k/k^* reaches 2.88 for $g_w > 0$, still less than that experimentally observed in a carbon nanotube [4]. If $|\lambda|/D > 1/4$, the interaction effect will be overestimated due to the deviation of Eq. (16) in approximating the near-wall velocity.

C. Flow through a porous medium

The advantage of our proposed LBM is its establishment at the particle level and applicability to porous media. The intrinsic permeability of a porous medium for conducting a single-phase fluid can be calculated by the Kozeny-Carman (KC) equation based on the assumption of Poiseuille-type
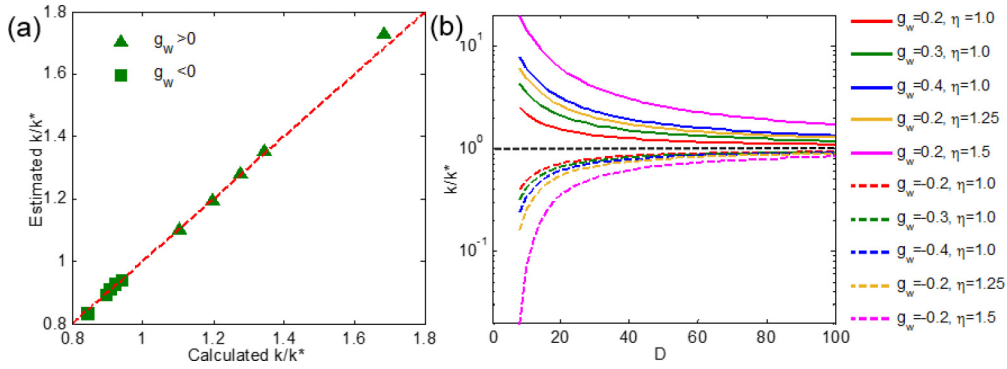
FIG. 7. Comparison of estimated k/k^* based on Eq. (21) and simulated k/k^* (a), and the variation of k/k^* with D as indicated by Eq. (21) (b) for the flow in a capillary tube.

flow through a bundle of tubes [67]

$$k = c_0 \phi R_h^2, \qquad (22)$$

where ϕ is the porosity, c_0 the shape factor taking into account pore geometry and streamline tortuosity, and R_h the hydraulic radius, i.e., the ratio of pore volume to pore surface area. However, in order to generalize Eq. (22) for a highly porous medium where the flow channels are largely interconnected, a modification is necessary by imposing an exponent m to ϕ, as follows:

$$k = c_0' \phi (D_{avg})^m D_{avg}^2, \qquad (23)$$

where c_0' is the new shape factor, D_{avg} the average pore diameter characterising the size of the flow channel, which replaces R_h for convenience in incorporating the slip length into Eq. (23), and ϕ the porosity as a function of D_{avg}.

The LBM simulations are conducted based on a two-dimensional porous medium. The four domain boundaries are all set as the periodic ones. Various shapes of grains can be used to generate the interconnected flow channels in

principle. However, in the presence of the F-S interaction, our simulations lead to significant spurious velocities using the proposed LBM approach. In addition to the jagged representation of curved boundaries, the insufficient isotropy in the calculation of density gradients, as pointed out in [63,66], can also result in the spurious currents in the vicinity of curved surfaces. As shown in Fig. 8, for circular grains, the remarkable vortices appear near the solid surface, which distinctly but unphysically change the streamline tortuosity and the flow process. Abnormally large velocities relative to the bulk flow arise around the solid surface, causing uncertainties in calculations of volume flux and permeability. Comparatively, for square grains, there are no such numerical vortices and the abnormally large velocities only occur at the corner of the square, which can be easily excluded. Therefore, the square grains are used in our simulations to avoid the poor approximation of the circular geometry and the resulting spurious current.

In Fig. 9(a), a porous medium packed with 60 unequal square grains is simulated over a domain of 1600×1600 in
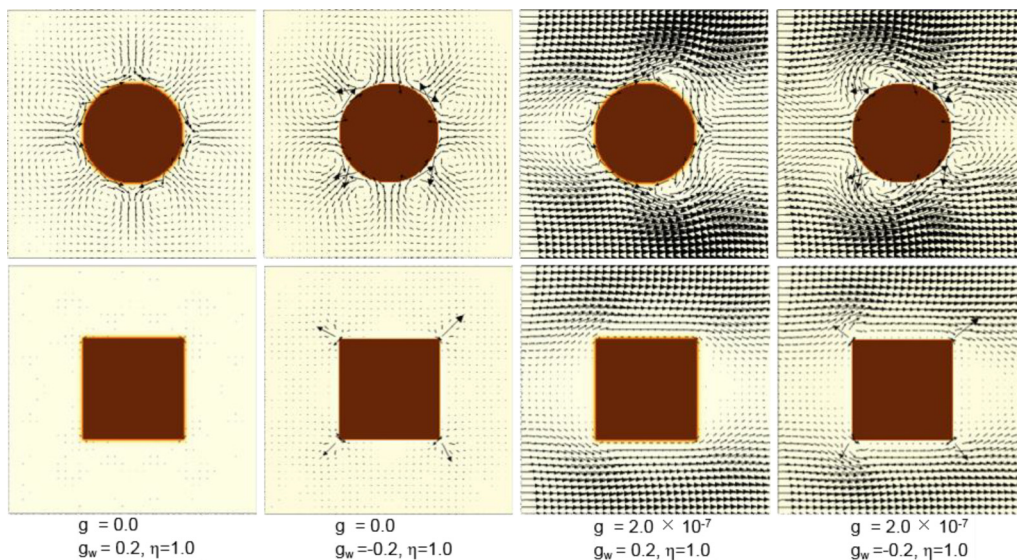

FIG. 8. Spurious velocities on the surface of circle and square grains, the magnitude of which is presented by the length of the arrows and follows the same scale.
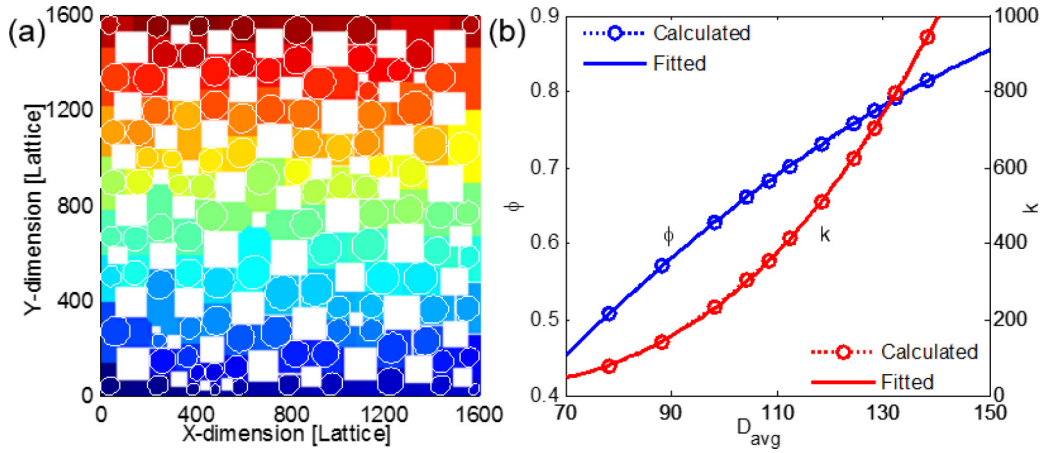
FIG. 9. A porous medium with square grains (white regions) and individual pore segments (colored regions) with the maximum circles (white lines) contained (a), and the relationship of $\phi(D_{\text{avg}})$ and validation of the modified KC equation in Eq. (23) (b). In panel (b), the fitted curves are $\phi(D_{\text{avg}}) = -2.316 \times 10^{-5} D_{\text{avg}}^2 + 0.010 D_{\text{avg}} - 0.141$ and $k(D_{\text{avg}}) = 0.0922 \phi^{2.800}(D_{\text{avg}}) D_{\text{avg}}^2$, respectively.

lattice units, with a porosity of 0.682. Using the watershed segmentation algorithm [68], the whole pore space is identified as a series of individual pore segments with various shapes. The size of each pore segment is defined as the diameter of the maximum circle contained in each segment. The diameters of these local maximum circles are averaged to quantify the average pore diameter, D_{avg}, appearing in Eq. (23). For the porous medium shown in Fig. 9(a), $D_{\text{avg}} = 103.7$ in lattice units. With the boundaries of each square extended outward to the pore space or inward to the solid space by a distance of ΔL_i but with the center of each square fixed, the average pore diameters can be determined as $(D_{\text{avg}} - 2\Delta L_i)$. Then porosities ϕ_i and permeabilities k_i ($k_i = q_{\text{no slip},i} \, \nu/g$) can be readily obtained. The data of $\phi(D_{\text{avg}})$ and $k(D_{\text{avg}})$ are shown in Fig. 9(b). These displayed relations can be excellently fitted by a polynomial function and Eq. (23), respectively. The validity of Eq. (23) for the given porous medium is justified. Simulations of the F-S interaction effect will be conducted on the porous medium shown in Fig. 9(a).

1. Slip length

The velocity field in a porous medium cannot be analytically approximated with the slip length incorporated as in a capillary tube. Nevertheless, it is found from the simulations in a capillary tube that the bulk flow affected by a slip length of λ is identical to that where the flow channel size increases by 2λ, and the maximum velocity in the bulk flow is most sensitive to the slip length. Based on these findings, the algorithm of slip length determination for the porous medium, used in our work, is described as the following:

(i) 95 points in the bulk flow region [as shown in Fig. 10(a)], with the local maximum velocities $u_i = f_i(D_{\text{avg}})$ ($i = 1, \ldots, 95$) for $g = 5.0 \times 10^{-7}$, are selected to link the slip lengths with the local velocities.

(ii) Extending the walls of each square outward to the pore space or inside to the solid space by a distance of d_k ($k = 1, \ldots, m$), but maintaining the position of each square, gives the average pore diameter ($D_{\text{avg}} - 2d_k$).

(iii) The velocities $u_{ik} = f_i(D_{\text{avg}} - 2d_k)$ at the points selected are obtained from the LBM simulations under the no-slip condition.

(iv) The data of $u_{ik} = f_i(D_{\text{avg}} - 2d_k)$ at each point selected are fitted by the polynomial functions $\hat{u}_i = F_i(D_{\text{avg}} - 2\hat{d})$. $\lambda = -\hat{d}$ is equivalent to the known slip length, and thus $\lambda = 0.5[F_i^{-1}(\hat{u}_i) - D_{\text{avg}}]$ (F_i^{-1} is the inverse function of F_i) gives the link between the slip lengths and the local velocities.

Using this algorithm, the simulated velocities in the presence of the F-S interaction, such as $g_w = \pm 0.2$ and $\eta = 1.0$, are used to calculate the slip lengths at each point selected, as shown in Fig. 10(a). The calculated slip lengths at the points selected fluctuate as expected but around a mean value ($\lambda = 0.890 \pm 0.213$, -0.602 ± 0.218 for $g_w = 0.2, -0.2$, respectively), which reasonably agrees with the implicit assumption of a uniform slip length around solid surfaces in a porous medium. The mean value of fluctuated slip lengths at these 95 points is taken to be the slip length for the given interaction parameters.

Figure 10(b) shows the nonlinear trends of simulated slip length with $|g_w|$ and η at $g = 5.0 \times 10^{-7}$ for the given porous medium. These nonlinear trends of slip length can be fitted by a single power law function as given by Eq. (17) with the fitting parameters, a_i, listed in Table II. The values of a_1 closer to 1 imply a less nonlinear increase with $|g_w|$, while the values of a_2 far larger than 1 indicate a more nonlinear increase with η. In particular, when $g_w < 0$, $a_1 < 1$ indicates a slow increase with $|g_w|$. a_1 and a_2 are both larger (showing a faster variation with $|g_w|$ and η) for $g_w > 0$ than those for $g_w < 0$ at the same magnitude of $|g_w|$ and η. Within the stability of the LBM used, the maximum (minimum) ratio of $|\lambda|/D_{\text{avg}}$ reaches 0.035 (0.013) for $g_w > 0$ ($g_w < 0$). Another important observation is that with the same values of interaction parameters, the slip length in porous media is smaller than that in capillary tubes [Fig. 5(b) and Fig. 10(b)]. Although the slip length is independent of the shear rate, it is affected by the pore geometry (and streamline tortuosity).
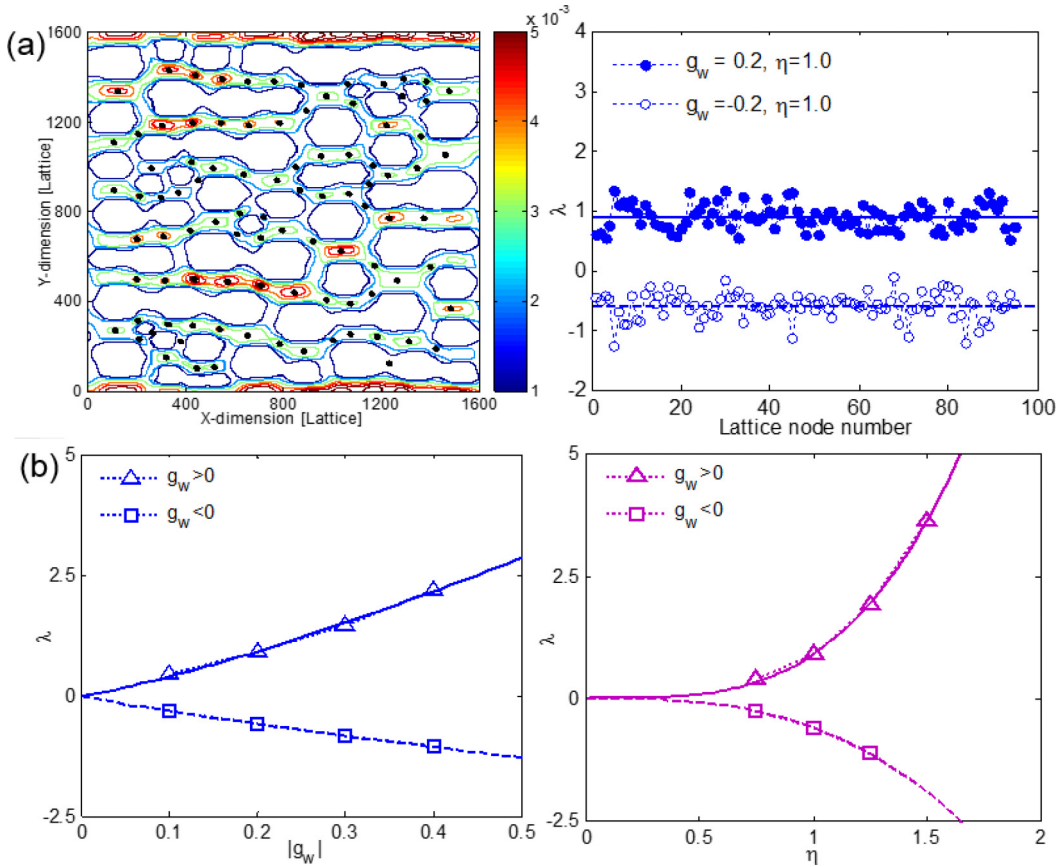
FIG. 10. Distribution of the velocity magnitude for $g = 5.0 \times 10^{-7}$ and selected points in the bulk flow region; slip lengths calculated on individual selected points for $g_w = \pm 0.2$ and $\eta = 1.0$ (a); dependencies of slip length on g_w for $\eta = 1.0$ and on η for $g_w = \pm 0.2$ (b). In panel (b), triangles and squares represent the simulated data for $g_w > 0$ and $g_w < 0$, respectively; solid and dashed curves are the fitted curves for $g_w > 0$ and $g_w < 0$, respectively.

2. Effect on permeability

The F-S interaction effect on average flow rate and permeability of a porous medium is also examined. As formulated in Eq. (18), the average flow rate is calculated here by the total volume flux divided by the area of cross section. The permeability ratio k/k^*, expressing the permeability change due to the F-S interaction, is calculated by Eq. (19). Note that the abnormally large velocities at the corner of the square grains are removed to alleviate the uncertainty in the calculations of volume flux and permeability.

The average flow rates versus the magnitudes of body force with respect to strength parameters, g_w and η, are presented in Fig. 11(a). The simulated data of average flow rate are proportional to the body force (zero body force intercept) for Reynolds numbers down to 0.120. The only change due to the F-S interaction lies in the slope which increases (decreases) for $g_w > 0$ ($g_w < 0$) compared with that under the no-slip condition. The slope change is nonlinear with g_w and η in a similar way. The zero force intercept means the absence of threshold applied force [3,40], consistent with the slip length (and then the effective pore size) independence of body force as found above. Again our proposed LBM model does not recover the phenomena of the pre-Darcy effect [48–50] and threshold pressure gradient [51–53] observed in shale and clay.

The F-S interaction effect on permeability can also be described by the permeability ratio as shown in Fig. 11(b). When $g_w > 0$ ($g_w < 0$), $k/k^* > 1$ ($k/k^* < 1$). k/k^* increases with g_w less nonlinearly but with η more nonlinearly. These trends can be well fitted by the power law function given in Eq. (20) with the fitted parameters, b_i, as listed in Table III. $b_0 > 0$ ($b_0 < 0$) links with $k/k^* > 1$ ($k/k^* < 1$) for $g_w > 0$ ($g_w < 0$). $b_2 > b_1$ suggests a faster increase of k/k^* with η than with $|g_w|$. Both b_1 and b_2 are larger for $g_w > 0$ than those for $g_w < 0$, indicating a stronger effect of repulsive interaction than that of attractive interaction at the same magnitude of strength parameters. The maximum permeability ratio achieved by the LBM model reaches about 1.25, comparable to that measured in a parallel-walled fracture [40] but far less than that observed in a carbon nanotube [4]. Another important finding is that, with the same interaction parameters, the permeability ratio in porous media is smaller than that in capillary tubes [Figs. 6(b) and 11(b)]. Thus, the F-S interaction effect on permeability is also affected by the pore geometry (and streamline tortuosity).

An analysis of a_i and b_i ($i = 1, 2$) for the fitted slip length and permeability ratio in Tables II and III gives that $a_2 \approx 2a_1 + 1$ and $b_2 \approx 2b_1 + 1$ are both reasonably justified, within the relative deviations of 6.11% and 6.16%, respectively, for the porous media. The similar variations of slip
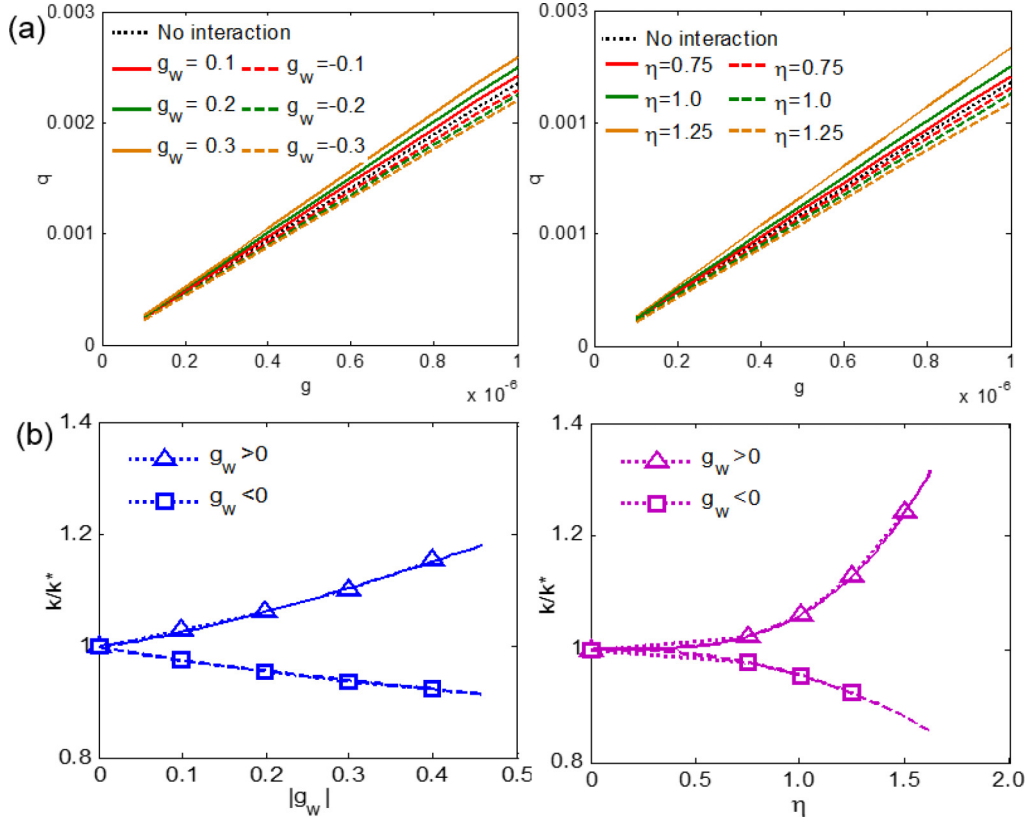
FIG. 11. Average flow rate as a function of g with respect to g_w for $\eta = 1.0$ and with respect to η for $g_w = \pm 0.2$ (a), and dependences of k/k^* on $|g_w|$ for $\eta = 1.0$ and on η for $g_w = \pm 0.2$ (b). In panel (b), triangles and squares represent the simulated data for $g_w > 0$ and $g_w < 0$, respectively; solid and dashed curves are the fitted curves for $g_w > 0$ and $g_w < 0$, respectively.

length and average flow rate versus magnitude of body force and permeability ratio with $|g_w|$ and η are also observed in Figs. 10(b) and 11. These results strongly imply the interconnection between $|g_w|$ and η in terms of their effects, and the possibility of combining the two free strength parameters, $|g_w|$ and η, into a single one.

The permeability ratio can also be estimated analytically based on the modified KC equation in Eq. (23) using the effective pore diameter, in addition to the simulated and fitted k/k^*. For a given porous medium with an average pore diameter of D_{avg}, a slip length of λ due to the F-S interaction equivalently results in an effective pore diameter of $(D_{avg} + 2\lambda)$ under the no-slip condition. On one hand, when $\lambda < 0$, the apparent solid surface is located inside the pore space. The near-wall velocity between the apparent solid surface and the real one is negligible, and the volume flux can be quite accurately quantified by that in a porous medium of $(D_{avg} + 2\lambda)$ under the no-slip condition. On the other hand, for $\lambda > 0$, the apparent solid surface lies inside the solid space. The extrapolated velocity between the apparent solid surface and the real one will contribute to an excessive volume flux. Nevertheless, if within a limited range of the ratio of $|\lambda|/D_{avg}$, the volume flux can also be reasonably quantified by that in a porous medium of $(D_{avg} + 2\lambda)$ under the no-slip condition. Thus $(D_{avg} + 2\lambda)$ is used here to replace D_{avg} in Eq. (23) to estimate the permeability in the presence of the F-S interaction. Thus the permeability ratio is estimated as

follows:

$$\frac{k}{k^*} = \frac{\phi(D_{avg} + 2\lambda)^m}{\phi(D_{avg})^m} \frac{(D_{avg} + 2\lambda)^2}{D_{avg}^2}. \qquad (24)$$

Figure 12(a) shows that with the simulated data of λ [Fig. 10(b)], the estimated k/k^* based on Eq. (24) agrees well with the simulated k/k^* [Fig. 11(b)] for $g_w < 0$, and is reasonably consistent with the simulated k/k^* [Fig. 11(b)] only up to $k/k^* \approx 1.1$ (that is, $|\lambda|/D_{avg} \approx 0.02$) and displays a remarkable overestimation for $g_w > 0$. Thus, Eq. (24) provides a fairly good way to estimate the permeability variation due to the F-S interaction when combined with Eq. (17). With reduced pore diameter and thus increased $|\lambda|/D_{avg}$, Eq. (24) can also be used to investigate the effect of pore diameter on the permeability ratio for the given strength parameters. Figure 12(b) illustrates that although k/k^* is greatly overestimated for $g_w > 0$ when $|\lambda|/D_{avg} > 0.02$, k/k^* shows a reliably nonlinear decrease with the decreased D_{avg} for $g_w < 0$, indicating a significant effect of the F-S interaction on permeability of the microporous media.

IV. CONCLUSIONS AND REMARKS

In this study, a mesoscopic single-phase LBM approach is established to describe the physics of the molecular F-S interaction and to assess the influence of fluid slip (damping) behavior on permeability estimation for shale oil and clay
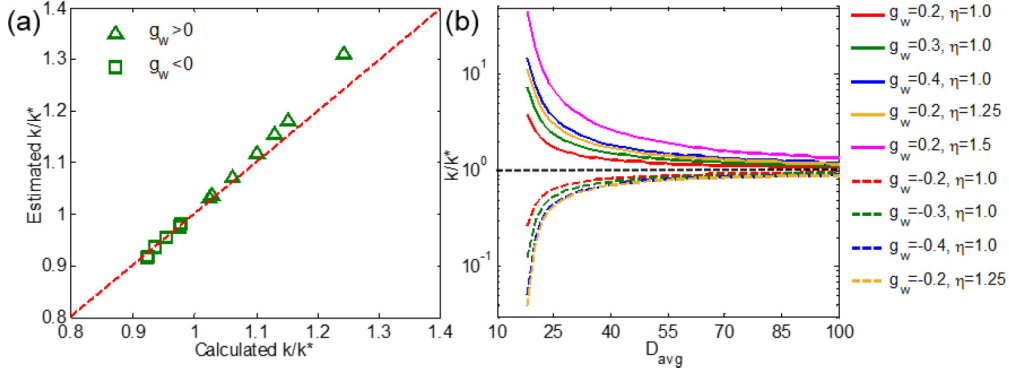
FIG. 12. Comparison of estimated k/k^* based on Eq. (24) and simulated k/k^* (a), and the variation of k/k^* with D_{avg} as indicated by Eq. (24) (b) for the flow through a porous medium.

water. The proposed model incorporates a midgrid bounce-back BC leading to a zero true slip, and a continuous and exponentially decaying F-S interaction force responsible for the apparent liquid slippage. The force function is applicable to porous media due to its establishment at the particle level. The positive (negative) slip lengths and thus fluid slip (damping) can be successfully recovered by the model, which is validated by the velocity profiles on hydrophobic and hydrophilic surfaces in a benchmark microchannel flow experiment.

The slip length, as observed in our simulations, is independent of shear rate (its constituents including body force, pore diameter, and kinematic viscosity), but depends on pore geometry (smaller in porous media than in capillary tubes). In both capillary tubes and porous media, the slip length and the permeability ratio follow a power law relation with interaction strength (and decay length), i.e., $\lambda \propto |g_w|^{a_1} \eta^{a_2}$ and $(k/k^* - 1) \propto |g_w|^{b_1} \eta^{b_2}$ with a_i and b_i ($i = 1, 2$) larger (indicating a stronger influence of repulsive interaction) in capillary tubes than those in porous media for $g_w > 0$ but comparable with each other for $g_w < 0$. The permeability ratio considering the slip length is also analytically estimated, and shows a nonlinear increase (decrease) as the pore diameter decreases, indicating the importance of F-S interaction for thin capillary tubes and microporous media.

The similar trends of velocity profile, slip length, and average flow rate versus magnitude of body force and permeability ratio, varying with $|g_w|$ and η, are observed in the simulation results. It was found that $a_2 \approx 2a_1 + 1$ and $b_2 \approx 2b_1 + 1$ both predicting the interconnection between $|g_w|$ and η in terms of the F-S interaction effect. From these results, it can be inferred that the two free strength parameters, $|g_w|$ and η, can be

combined into a single one. Moreover, the power law relation, $\lambda \propto |g_w|^{a_1} \eta^{a_2}$, can be rewritten as $\lambda/\eta \propto (|g_w|\eta^2)^{a_1}$, where λ/η and $|g_w|\eta^2$ are two dimensionless numbers equivalent to that in Eq. (13). The proposed model does not recover the phenomena of the pre-Darcy effect [48–50] and threshold pressure gradient [51–53] in shale and clay, which, however, is consistent with the independence of slip length (and then the effective pore size) on body force.

As the F-S interaction strengthens, the proposed LBM model tends to be less stable due to the steep density gradient. The maximum permeability ratio achieved by the LBM model reaches about 1.7 in capillary tubes and about 1.25 in porous media, which are far less than that experimentally observed in a carbon nanotube [4]. Therefore the numerical stability of the proposed LBM model needs to be improved further. The LBM simulations in the presence of the F-S interaction also lead to significant spurious velocities for curved solid surfaces, which hinders the investigations of pore geometry effect on slip length and permeability ratio in porous media packed with different shapes of solid grains. The issue of spurious velocity of the proposed LBM model needs to be resolved properly.

ACKNOWLEDGMENTS

APPENDIX A: DISCRETE VELOCITIES

$$\mathrm{D_2Q_9}: \mathbf{e}_0 \sim 8 = \begin{bmatrix} 0 & 1 & 0 & -1 & 0 & 1 & -1 & -1 & 1 \\ 0 & 0 & 1 & 0 & -1 & 1 & 1 & -1 & -1 \end{bmatrix}.$$

$$\mathrm{D_3Q_{19}}: \mathbf{e}_0 \sim 18 = \begin{bmatrix} 0 & 1 & -1 & 0 & 0 & 0 & 0 & 1 & -1 & 1 & -1 & 1 & -1 & 1 & -1 & 0 & 0 & 0 & 0 \\ 0 & 0 & 0 & 1 & -1 & 0 & 0 & 1 & -1 & -1 & 1 & 0 & 0 & 0 & 0 & 1 & -1 & 1 & -1 \\ 0 & 0 & 0 & 0 & 0 & 1 & -1 & 0 & 0 & 0 & 0 & 1 & -1 & -1 & 1 & 1 & -1 & -1 & 1 \end{bmatrix}$$

APPENDIX B: WEIGHT COEFFICIENTS

$$D_2Q_9: \quad w_{0\sim8} = \left[\frac{4}{9}, \frac{1}{9}, \frac{1}{9}, \frac{1}{9}, \frac{1}{9}, \frac{1}{36}, \frac{1}{36}, \frac{1}{36}, \frac{1}{36}\right].$$

$$D_3Q_{19}: \quad w_{0\sim18} = \left[\frac{1}{3}, \frac{1}{18}, \frac{1}{18}, \frac{1}{18}, \frac{1}{18}, \frac{1}{18}, \frac{1}{18}, \frac{1}{36}, \frac{1}{36}, \frac{1}{36}, \frac{1}{36}, \frac{1}{36}, \frac{1}{36}, \frac{1}{36}, \frac{1}{36}, \frac{1}{36}, \frac{1}{36}, \frac{1}{36}, \frac{1}{36}\right].$$

[1] G. Batchelor, *An Introduction to Fluid Dynamics* (Cambridge University Press, Cambridge, 1970).

[2] E. Schnell, Slippage of water over nonwettable surfaces, J. Appl. Phys. **27**, 1149 (1956).

[3] N. V. Churaev, V. D. Sobolev, and A. N. Somov, Slippage of liquids over lyophobic solid surfaces, J. Colloid Interf. Sci. **97**, 574 (1984).

[4] J. A. Thomas and A. J. H. McGaughey, Water Flow in Carbon Nanotubes: Transition to Subcontinuum Transport, Phys. Rev. Lett. **102**, 184502 (2009).

[5] D. C. Tretheway and C. D. Meinhart, Apparent fluid slip at hydrophobic microchannel walls, Phys. Fluids **14**, L9 (2002).

[6] P. Joseph and P. Tabeling, Direct measurement of the apparent slip length, Phys. Rev. E **71**, 035303 (2005).

[7] J. Ou and J. P. Rothstein, Direct velocity measurements of the flow past drag-reducing ultrahydrophobic surfaces, Phys. Fluids **17**, 103606 (2005).

[8] Y. Zhu and S. Granick, Rate-Dependent Slip of Newtonian Liquid at Smooth Surfaces, Phys. Rev. Lett. **87**, 096105 (2001).

[9] V. S. J. Craig, C. Neto, and D. R. M. Williams, Shear-Dependent Boundary Slip in an Aqueous Newtonian Liquid, Phys. Rev. Lett. **87**, 054504 (2001).

[10] C. Cottin-Bizonne, B. Cross, A. Steinberger, and E. Charlaix, Boundary Slip on Smooth Hydrophobic Surfaces: Intrinsic Effects and Possible Artifacts, Phys. Rev. Lett. **94**, 056102 (2005).

[11] J.-L. Barrat and L. Bocquet, Large Slip Effect at A Nonwetting Fluid-Solid Interface, Phys. Rev. Lett. **82**, 4671 (1999).

[12] D. M. Huang, C. Sendner, D. Horinek, R. R. Netz, and L. Bocquet, Water Slippage versus Contact Angle: A Quasiuniversal Relationship, Phys. Rev. Lett. **101**, 226101 (2008).

[13] D. M. Huang, C. Sendner, D. Horinek, R. R. Netz, and L. Bocquet, Wettability effect on nanoconfined water flow, Proc. Natl. Acad. Sci. USA **114**, 3358 (2017).

[14] J. Harting, C. Kunert, and H. J. Herrmann, Lattice Boltzmann simulations of apparent slip in hydrophobic microchannels, Europhys. Lett. **75**, 328 (2006).

[15] R. Benzi, L. Biferale, M. Sbragaglia, S. Succi, and F. Toschi, Mesoscopic two-phase model for describing apparent slip in micro-channel flows, Europhys. Lett. **74**, 651 (2006).

[16] J. Zhang, and D. Y. Kwok, Apparent slip over a solid-liquid interface with a no-slip boundary condition, Phys. Rev. E **70**, 056701 (2004).

[17] E. Lauga, M. P. Brenner, and H. A. Stone, Microfluidics: The no-slip boundary condition, in *Springer Handbook of Experimental Fluid Mechanics* (Springer, Heidelberg, 2005), pp. 1219–1240.

[18] C. Neto, D. R. Evans, E. Bonaccurso, H.-J. Butt, and V. S. J. Craig, Boundary slip in Newtonian liquids: A review of experimental studies, Rep. Prog. Phys. **68**, 2859 (2005).

[19] E. Ruckenstein and P. Rajora, On the no-slip boundary condition of hydrodynamics, J. Colloid Interf. Sci. **96**, 488 (1983).

[20] B. V. Derjaguin and N. V. Churaev, Structure of water in thin layers, Langmuir **3**, 607 (1987).

[21] N. Ishida, T. Inoue, M. Miyahara, and K. Higashitani, Nano bubbles on a hydrophobic surface in water observed by tapping-mode atomic force microscopy, Langmuir **16**, 6377 (2000).

[22] Y. Shangjiong, S. M. Dammer, N. Bremond, H. J. W. Zandvliet, E. Stefan Kooij, and D. Lohse, Characterization of nanobubbles on hydrophobic surfaces in water, Langmuir **23**, 7072 (2007).

[23] O. I. Vinogradova, Slippage of water over hydrophobic surfaces, Int. J. Miner. Process. **56**, 31 (1999).

[24] D. C. Tretheway and C. D. Meinhart, A generating mechanism for apparent fluid slip in hydrophobic microchannels, Phys. Fluids **16**, 1509 (2004).

[25] T. D. Blake, Slip between a liquid and a solid: D. M. Tolstoi's theory reconsidered, Colloid. Surf. **47**, 135 (1990).

[26] G. McHale and M. I. Newton, Surface roughness and interfacial slip boundary condition for quartz crystal microbalances, J. Appl. Phys. **95**, 373 (2004).

[27] S. C. Yang and L. B. Fang, Effect of surface roughness on slip flows in hydrophobic and hydrophilic microchannels by molecular dynamics simulation, Mol. Simulat. **31**, 971 (2005).

[28] A. M. J. Davis and E. Lauga, Geometric transition in friction for flow over a bubble mattress, Phys. Fluids **21**, 011701 (2009).

[29] R. Pit, H. Hervet, and L. Léger, Direct Experimental Evidence of Slip in Hexaecane: Solid Interfaces, Phys. Rev. Lett. **85**, 980 (2000).

[30] E. Bonaccurso, M. Kappl, and H.-J. Butt, Hydrodynamic Force Measurements: Boundary Slip of Water on Hydrophilic Surfaces and Electrokinetic Effects, Phys. Rev. Lett. **88**, 076103 (2002).

[31] T. A. Ho, D. V. Papavassiliou, L. L. Lee, and A. Striolo, Liquid water can slip on a hydrophilic surface, Proc. Natl. Acad. Sci. USA **108**, 16170 (2011).

[32] J. Baudry, E. Charlaix, A. Tonck, and D. Mazuyer, Experimental evidence for a large slip effect at a nonwetting fluid-solid interface, Langmuir **17**, 5232 (2001).

[33] O. I. Vinogradova, Implications of hydrophobic slippage for the dynamic measurements of hydrophobic forces, Langmuir **14**, 2827 (1998).

[34] J. Israelachvili and R. Pashley, The hydrophobic interaction is long range, decaying exponentially with distance, Nature (London) **300**, 341 (1982).

[35] P. M. Claesson and H. K. Christenson, Very long range attractive forces between uncharged hydrocarbon and fluorocarbon surfaces in water, J. Phys. Chem. **92**, 1650 (1988).

[36] E. Ruckenstein and N. Churaev, A possible hydrodynamic origin of the forces of hydrophobic attraction, J. Colloid Interf. Sci. **147**, 535 (1991).

[37] F. Javadpour, M. McClure, and M. E. Naraghi, Slip-corrected liquid permeability and its effect on hydraulic fracturing and fluid loss in shale, Fuel **160**, 549 (2015).

[38] A. Afsharpoor and F. Javadpour, Liquid slip flow in a network of shale noncircular nanopores, Fuel **180**, 580 (2016).

[39] S. Wang, F. Javadpour, and Q. Feng, Molecular dynamics simulations of oil transport through inorganic nanopores in shale, Fuel **171**, 74 (2016).

[40] H. B. Lee, I. W. Yeo, and K. K. Lee, Water flow and slip on NAPL-wetted surfaces of a parallel-walled fracture, Geophys. Res. Lett. **34**, L19401 (2007).

[41] H. B. Lee, I. W. Yeo, S. H. Ji, and K. K. Lee, Wettability-dependent DNAPL migration in a rough-walled fracture, J. Contam. Hydrol. **113**, 44 (2010).

[42] H. B. Lee, I. W. Yeo, and K. K. Lee, Fluid flow through rough-walled rock fractures with hydrophobic surfaces, Geosci. J. **18**, 375 (2014).

[43] D.-X. Liu, X.-A. Yue, L.-M. Wang, J.-R. Hou, and J.-H. Zhang, Model study on the irreducible water saturation by centrifuge experiments, J. Petrol. Sci. Eng. **53**, 77 (2006).

[44] B. Z. Shang, J. G. Hamman, H. Chen, and D. H. Caldwell, A model to correlate permeability with efficient porosity and irreducible water saturation, in *SPE Annual Technical Conference and Exhibition, 5-8 October 2003, Denver, Colorado, USA* (SPE, 2003), doi:10.2118/84303-MS.

[45] M. Izadi and A. Ghalambor, A new approach in permeability and hydraulic-flow-unit determination, in SPE Reservoir Evaluation and Engineering (SPE, 2013), p. 257.

[46] X. Chen and G. Yao, An improved model for permeability estimation in low permeable porous media based on fractal geometry and modified Hagen-Poiseuille flow, Fuel **210**, 748 (2017).

[47] Y. Cheng, C. Zhang, and L. Q. Zhu, A fractal irreducible water saturation model for capillary tubes and its application in tight gas reservoir, J. Petrol. Sci. Eng. **159**, 731 (2017).

[48] B. Zeng, L. Cheng, and C. Li, Low velocity non-linear flow in ultra-low permeability reservoir, J. Petrol. Sci. Eng. **80**, 1 (2012).

[49] F. Siddiqui, M. Y. Soliman, W. House, and A. Ibragimov, Pre-Darcy flow revisited under experimental investigation, J. Anal. Sci. Technol. **7**, 2 (2016).

[50] M. Dejam, H. Hassanzadeh, and Z. Chen, Pre-Darcy flow in porous media, Water Resources Res. **53**, 8187 (2017).

[51] A. Prada and F. Civan, Modification of Darcy's law for the threshold pressure gradient, J. Petrol. Sci. Eng. **22**, 237 (1999).

[52] F. Hao, L. S. Cheng, O. Hassan, *et al.*, Threshold pressure gradient in ultra-low permeability reservoirs, Petrol. Sci. Technol. **26**, 1024 (2008).

[53] S. Wang, W. Zhu, X. Qian, *et al.*, Study of threshold gradient for compacted clays based on effective aperture, Environ. Earth Sci. **75**, 693 (2016).

[54] G. Longmuir, Pre-Darcy flow: A missing piece of the improved oil recovery puzzle, in *2004 SPE/DOE Fourteenth Symposium on Improved Oil Recovery, Tulsa, Oklahoma* (SPE, 2004), doi:10.2118/89433-MS.

[55] S. Succi, *The Lattice Boltzmann Equation: For Fluid Dynamics and Beyond* (Oxford University Press, New York, 2001).

[56] S. Succi, Mesoscopic Modeling of Slip Motion at Fluid-Solid Interfaces with Heterogeneous Catalysis, Phys. Rev. Lett. **89**, 064502 (2002).

[57] L. Zhu, D. Tretheway, L. Petzold, and C. Meinhart, Simulation of fluid slip at 3D hydrophobic microchannel walls by the lattice Boltzmann method, J. Comput. Phys. **202**, 181 (2005).

[58] C. Y. Lim, C. Shu, X. D. Niu, and Y. T. Chew, Application of lattice Boltzmann method to simulate microchannel flows, Phys. Fluids **14**, 2299 (2002).

[59] G. H. Tang, W. Q. Tao, and Y. L. He, Lattice Boltzmann method for gaseous microflows using kinetic theory boundary conditions, Phys. Fluids **17**, 058101 (2005).

[60] H. Huang, M. C. Sukop, and X. Lu, *Multiphase Lattice Boltzmann Methods: Theory and Application* (John Wiley and Sons, Ltd., West Sussex, 2015).

[61] X. Shan and H. Chen, Lattice Boltzmann model for simulating flows with multiple phases and components, Phys. Rev. E **47**, 1815 (1993).

[62] H. Huang, M. Krafczyk, and X. Lu, Forcing term in single-phase and Shan-Chen-type multiphase lattice Boltzmann models, Phys. Rev. E **84**, 046710 (2011).

[63] M. L. Porter, E. T. Coon, Q. Kang, J. D. Moulton, and J. W. Carey, Multicomponent interparticle-potential lattice Boltzmann model for fluids with large viscosity ratios, Phys. Rev. E **86**, 036701 (2012).

[64] X. He, X. Shan, and G. D. Doolen, Discrete Boltzmann equation model for nonideal gases, Phys. Rev. E **57**, R13(R) (1998).

[65] C. Pan, L. S. Luo, and C. T. Miller, An evaluation of lattice Boltzmann schemes for porous medium flow simulation, Comput. Fluids **35**, 898 (2006).

[66] X. Shan, Analysis and reduction of the spurious current in a class of multiphase lattice Boltzmann models, Phys. Rev. E **73**, 047701 (2006).

[67] P. H. Nelson, Permeability-porosity relationships in sedimentary rocks, The Log Analyst **35**, 38 (1994), https://www.onepetro.org/journal-paper/SPWLA-1994-v35n3a4.

[68] A. Rabbani, S. Jamshidi, and S. Salehi, An automated simple algorithm for realistic pore network extraction from micro-tomography images, J. Petrol. Sci. Eng. **123**, 164 (2014).